

SCAN-BEST: Efficient Sub-6GHz-Aided Near-field Beam Selection with Formal Reliability Guarantees

Weicao Deng, *Graduate Student Member, IEEE*, Binpu Shi, *Graduate Student Member, IEEE*,
Min Li, *Member, IEEE*, and Osvaldo Simeone, *Fellow, IEEE*

Abstract—As millimeter-wave (mmWave) multiple-input multiple-output (MIMO) systems continue to incorporate larger antenna arrays, the range of near-field propagation expands, making it more likely for users close to the transmitter to fall within the near-field regime. Traditional far-field beam training methods are no longer effective in this context. Additionally, near-field beam training presents challenges, since the training codebook must account for both angular and distance dimensions, leading to large codebook sizes. To reduce the in-band training overhead, we propose the Sub-6G Channel-Aided Near-field BEam SelecTion (SCAN-BEST) framework, which is motivated by the spatial-temporal congruence between sub-6 GHz (sub-6G) and mmWave channels. SCAN-BEST utilizes preprocessed sub-6G channel estimates as input, and employs a convolutional neural network (CNN) to predict the probability of each beam being optimal within the near-field beam training codebook. Given the prediction uncertainty arising from the variance between sub-6G and mmWave channels, we introduce a conformal risk control (CRC)-based module that generates a set of beam candidates for further limited in-band training, enabling the final beam selection to formally meet user-defined target coverage rate. Numerical results confirm the theoretical properties of SCAN-BEST in terms of the achieved coverage rate of the beam candidates and various metrics. Moreover, SCAN-BEST enjoys good scalability and robustness to various sub-6G system configurations, including to the sizes of calibration datasets.

Index Terms—Near-field, beam selection, conformal risk control, sub-6G channel, deep learning.

I. INTRODUCTION

Millimeter-wave (mmWave) and extremely large-scale massive multiple-input multiple-output (XL-MIMO) are recognized as key enablers for 6G communication systems [1], [2]. However, their adoption introduces unique challenges due to the high operating frequencies and to the large antenna array sizes, which result in a substantial increase in the Rayleigh distance—from a few meters to several hundred meters [3]. This significantly expands the near-field region, where electromagnetic waves must be accurately modeled

The work of Osvaldo Simeone was partially supported by the European Union’s Horizon Europe project CENTRIC (101096379), by the Open Fellowships of the EPSRC (EP/W024101/1) and by the EPSRC project (EP/X011852/1).

Weicao Deng, Binpu Shi, and Min Li are with the College of Information Science and Electronic Engineering and Zhejiang Provincial Key Laboratory of Multi-Modal Communication Networks and Intelligent Information Processing, Zhejiang University, Hangzhou 310027, China (e-mail: {caowd, bp.shi, min.li}@zju.edu.cn). (*Corresponding authors: Min Li.*)

Osvaldo Simeone is with the King’s Communications, Learning & Information Processing (KCLIP) lab within the Centre for Intelligent Information Processing Systems (CIIPS), Department of Engineering, King’s College London, London WC2R 2LS, U.K. (e-mail: osvaldo.simeone@kcl.ac.uk).

using spherical wavefronts rather than planar approximations [4]. Communication quality in this regime becomes highly susceptible to blockages [5], [6], presenting significant challenges for channel state information (CSI) acquisition and beamforming design.

This work explores the idea of using sub-6 GHz (sub-6G) channel data to enhance mmWave communication. As illustrated in Fig. 1, sub-6G and mmWave channels exhibit similar power delay profiles (PDPs) [7], [8]. This congruence suggests the potential to extract both angular and distance information from sub-6G channels to facilitate near-field beam selection. Nonetheless, significant challenges remain due to the inherent differences between sub-6G and mmWave channels, such as variations in path parameters and discrepancies in angular and temporal resolutions. These differences introduce uncertainties when mapping sub-6G channel data to mmWave beams, as illustrated by the dominant path differences in Fig. 1b. Additionally, ensuring guaranteed performance for near-field beam selection remains an open research question and a critical challenge.

A. Related Works and Motivations

To address these challenges, a significant number of works [9]–[13] have focused on the angle and distance characteristics of near-field channels, proposing various beam training approaches. For instance, reference [9] introduced on-grid/off-grid polar-domain simultaneous orthogonal matching pursuit (OMP) channel estimation methods that exploit the polar-domain sparsity of near-field channels. Reference [10] developed a two-phase beam training scheme that divides the two-dimensional search in the polar-domain codebook into two sequential angular and distance domain searches. Similarly, reference [11] proposed a two-stage hierarchical beam training method. In the first stage, the central sub-array is used to perform a coarse search for the user direction in the angular domain. In the second stage, a fine-grained search for the user’s direction and distance is conducted in the polar domain.

Inspired by the integration of wireless communication and artificial intelligence (AI), reference [12] proposed frameworks to predict the optimal angle and distance using extensive near-field beam training. Likewise, reference [13] developed a framework that leverages received signals from the far-field wide beam training. These studies rely solely on in-band measurements and often struggle to achieve optimal performance under a limited pilot budget or low signal-to-noise ratio (SNR) conditions.

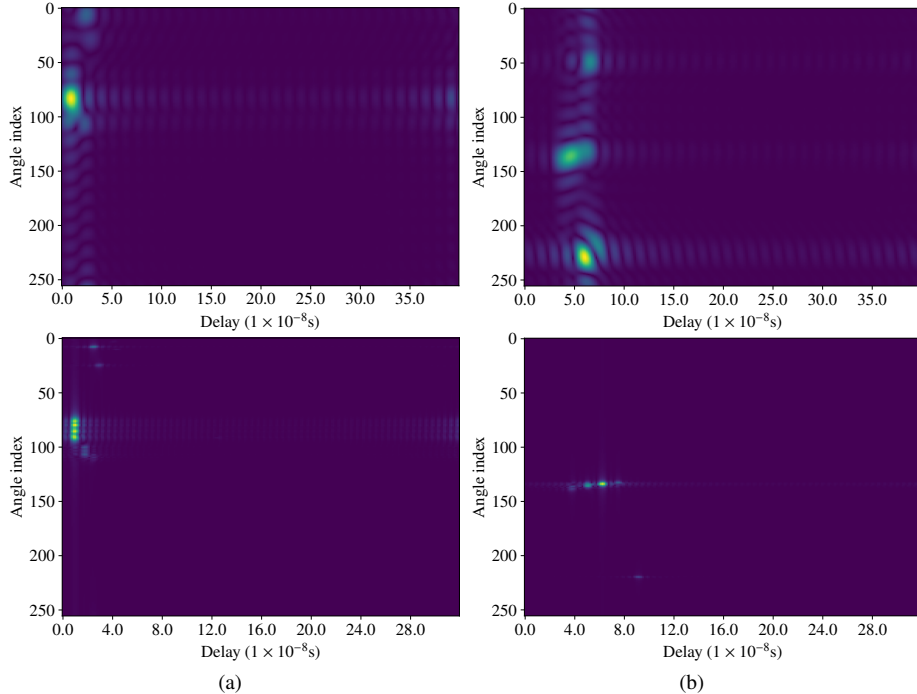


Fig. 1. An illustration of spatial and temporal correlation between sub-6G and mmWave channels. Each column represents a pair of sub-6G (upper row) and mmWave (lower row) augmented angle and delay profiles. The first column describes a line-of-sight (LoS) condition, while the second column represents a non-LoS (NLoS) condition [14].

Several studies [15]–[18] have utilized the angular domain congruence between sub-6G and mmWave channels to assist the far-field beam selection or beamforming. Building on [15], reference [19] proposed a complex simultaneous logit-weighted block OMP algorithm for near-field channel estimation, which leverages the angular domain congruence between sub-6G and mmWave channel to design the training codebook and assign weights. However, in the context of near-field beamforming or channel estimation, it’s not just the angle information that is requisite; distance information is similarly necessary.

Conformal risk control (CRC) is a widely used technique for quantifying model uncertainty and providing risk guarantees, which has been extensively studied in numerous previous works in mathematics and statistics [20]–[22]. With the recent advancements in AI, CRC has also emerged a valuable tool for enhancing the reliability of AI systems [23]–[25]. For example, reference [26] developed a novel delay-adaptive spiking neural network (SNN) based inference approach that ensures reliable decision-making at input-dependent stopping times. Reference [27] introduced a novel probabilistic time series-conformal risk prediction, which assembles multiple prototype trajectories sampled from a sequence model, to effectively represent forking uncertainties.

In the context wireless communication, references [28] was the first to explore the application of conformal prediction (CP), a precursor of CRC [22], in the design of AI for communication systems, with focus on demodulation, modulation classification, and channel prediction. Additionally, reference [29] investigated federated CP in a wireless setting, proposing a novel wireless federated CP framework for federated reliable

inference. Reference [30] further proposed a novel method for solving multi-label classification problems under both communication constraints and performance guarantees in distributed sensor networks.

B. Main Contributions

The correlation between sub-6G and mmWave channels illustrated in Fig. 1 offers promising potential for enabling low-overhead near-field beam selection, surpassing traditional in-band schemes. However, the non-negligible discrepancies between these two frequency bands introduce substantial uncertainty in predicting mmWave near-field beams based on sub-6G information. To address this challenge, we develop Sub-6GHz Channel Aided Near-field BEam Selection (SCAN-BEST), a framework combining deep learning for beam prediction with CRC to ensure reliability guarantee. Our main contributions are summarized as follows:

- 1) We develop the SCAN-BEST, a framework that enables reliable sub-6G channel-aided near-field beam selection. SCAN-BEST begins with an efficient preprocessing step to enhance the structural representation of the angular and distance information in the raw sub-6G channel estimates. A two-dimensional (2D) convolutional neural network (CNN) is then employed to predict the probabilities of optimal near-field beams. Subsequently, a CRC-based scheme efficiently constructs a near-field candidate beam set that formally meets a target coverage rate. This allows the network to guarantee that a user-defined level of suboptimality in beam selection is ensured with any pre-defined probability. Finally, additional limited mmWave

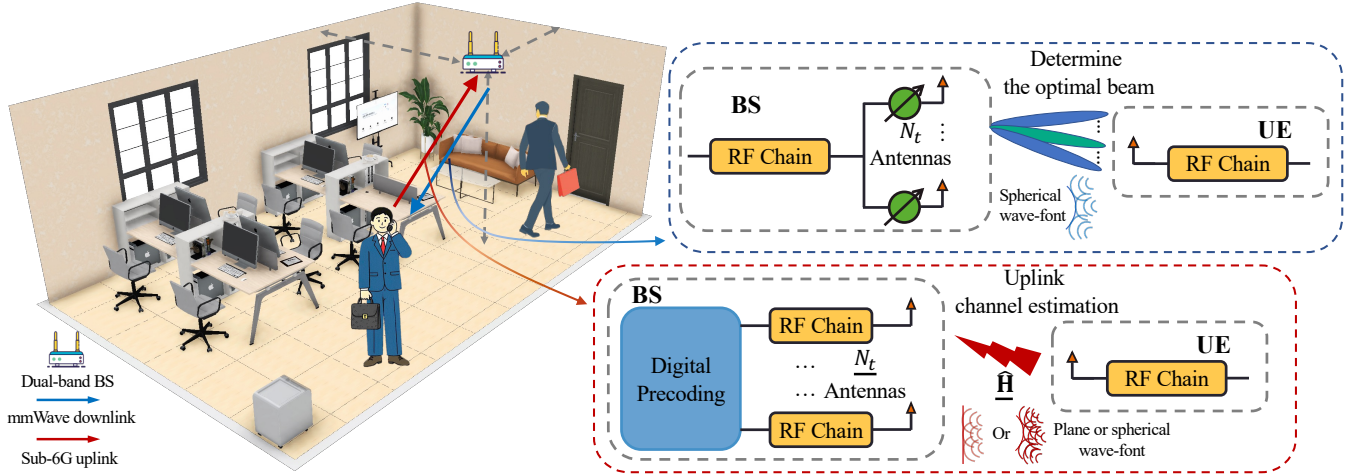


Fig. 2. An illustration of system model and beamforming architecture.

beam training is carried out to identify the near-field beam.

- 2) We conduct comprehensive numerical simulations to validate the efficiency of SCAN-BEST by comparing it with various mmWave and sub-6G-based baselines. The calibration performance is evaluated across different target coverage rates and calibration dataset sizes. Furthermore, we examine the scalability of SCAN-BEST by varying the quality of sub-6G data, including changes in the number of sub-6G antennas and the power levels in sub-6G channel estimation.

The remainder of this paper is organized as follows. Section II describes the system model and formulates the problem of sub-6G channel-aided near-field beam selection as well as its calibration. Section III elaborates on the proposed SCAN-BEST framework from its implementation. In Section IV-A, we present and discuss the numerical results to validate the effectiveness of SCAN-BEST. Section V provides conclusions for this paper.

Notations: Scalars, vectors and matrices are respectively denoted by lower/upper case, boldface lower case and boldface upper case letters. Notation \mathbf{I}_m represents an $m \times m$ identity matrix. $\mathcal{CN}(0, \sigma^2)$ is a zero-mean complex Gaussian distribution with variance σ^2 . The function $\text{card}(\mathcal{X})$ returns the cardinality of set \mathcal{X} . The notation $A \times B$ is also used for the Cartesian product of the sets $\{1, 2, \dots, A\}$ and $\{1, 2, \dots, B\}$ with integers A and B . Moreover, to distinguish between the sub-6G system and mmWave system, we use $\underline{(\cdot)}$ to indicate parameters corresponding to the sub-6G system, as exemplified by \underline{x} .

II. SYSTEM MODEL AND PROBLEM FORMULATION

As depicted in Fig. 2, as in [15]–[17], we consider a dual-band system comprising a BS and single UE. Both the BS and UE are equipped with two transceivers that operate in sub-6G frequencies and mmWave frequencies, respectively. The UE is assumed to have a single antenna in both mmWave and sub-6G frequencies. As for the BS, the mmWave system

is equipped a uniform linear array (ULA) with N_t half-wavelength antennas, and it adopts a fully analog beamforming architecture. In contrast, its sub-6G system is equipped with N_t half-wavelength ULA antennas, and it employs a fully digital beamforming architecture. In the rest of this section, we will define the mmWave and sub-6G radio interfaces, as well as the problem definition.

A. MmWave Downlink Communication and Channel Model

We consider a wideband mmWave orthogonal frequency division multiplex (OFDM) system operating at the center frequency f_c with a total system bandwidth W and K sub-carriers. The sampling period T_s is given by $T_s = 1/W$, and the number of channel taps at the resolution T_s is denoted as D . The signal transmitted at the k -th subcarrier $s_{t,k} \in \mathbb{C}$ follows the complex Gaussian distribution $\mathcal{CN}(0, P_t/K)$ with P_t being the total transmitting power. Denote as \mathbf{f} the analog beam applied by the BS, the received signal of the UE at the k -th subcarrier $y_k \in \mathbb{C}$ can be written as [31]

$$y_k = \mathbf{h}_k^H \mathbf{f} s_{t,k} + n_k, \quad (1)$$

where $\mathbf{h}_k^H \in \mathbb{C}^{1 \times N_t}$ denotes the frequency-domain channel from the BS to the UE at the k -th subcarrier, and $n_k \sim \mathcal{CN}(0, \sigma_n^2)$ is the additive noise with the variance σ_n^2 .

We adopt a wideband geometric channel model consisting of a total of L paths between the BS and the UE. To account for large arrays, we model the extended near-field range via spherical wave-fronts [3]. The channel gain, angle of departure (AoD), and time of arrival (ToA) of the l -th path between the BS and the UE are denoted by g_l , θ_l , and τ_l , respectively. Furthermore, if the l -th path is in line of sight (LOS), the additional path parameter r_l is used to denote the distance between the BS and the UE, while otherwise, r_l denotes the distance between the BS and the scatterer in the l -th path of the UE. Overall, the delay- d mmWave channel tap from the BS to UE, denoted as $\mathbf{h}_d^H \in \mathbb{C}^{1 \times N_t}$, is given by [15]

$$\mathbf{h}_d^H = \sqrt{N_t} \sum_{l=1}^L g_l p(dT_s - \tau_l) \mathbf{b}^H(\theta_l, r_l), \quad (2)$$

for $d = 1, \dots, D$, where $p(\cdot)$ denote the pulse-shaping filter, and the steering vector $\mathbf{b}^H(\theta_l, r_l)$ is given by

$$\mathbf{b}^H(\theta_l, r_l) = \frac{1}{N_t} [e^{-j2\pi(r_l^{(0)} - r_l)}, \dots, e^{-j2\pi(r_l^{(N_t-1)} - r_l)}], \quad (3)$$

with $r_l^{(n)} = \sqrt{r_l^2 + \delta^{(n)2}(\lambda/2)^2 - r_l\theta_l\delta^{(n)}\lambda}$, with $\delta^{(n)} = (2n - N_t - 1)/2$ [3]. Based on the delay- d channel tap in (2), the frequency-domain mmWave channel at the k -th subcarrier, $\mathbf{h}_k^H \in \mathbb{C}^{1 \times N_t}$ is given by

$$\mathbf{h}_k^H = \sum_{d=1}^D \mathbf{h}_d^H e^{-j\frac{2\pi k}{K}d}, \quad (4)$$

for $k = 1, \dots, K$. For notational convenience, we denote the overall frequency-domain mmWave OFDM channel as $\mathbf{H} \triangleq [\mathbf{h}_1, \dots, \mathbf{h}_K]^H$.

B. Sub-6G Uplink Channel Estimation and Channel Model

The sub-6G link between BS and UE operates at the center frequency f_c , with a total bandwidth W , number of subcarriers K , sampling period $T_s = 1/W$, and number of channel taps D . Due to the more abundant scattering and diffraction of sub-6G propagation with respect to (w.r.t.) the mmWave band, there typically exist $\underline{L} > L$ paths between the BS and UE [7], [15]. We denote the gain, angle of arrival (AoA), time of arrival (ToA) of the l -th channel path with g_l , $\underline{\theta}_l$, and τ_l , respectively. Due to the shorter Rayleigh distance of the sub-6G system compared to the mmWave system, the UE is likely to be located in either the far-field or near-field region of the sub-6G system. Thus, similar to the latest work [19], the sub-6G channel between the BS and the UE is modeled under two cases.

When the UE is located in the far-field region, the delay- d sub-6G channel tap from the UE to BS $\underline{\mathbf{h}}_d \in \mathbb{C}^{N_t \times 1}$ is given by [15]

$$\underline{\mathbf{h}}_d = \sum_{l=1}^{\underline{L}} g_l p(dT_s - \tau_l) \underline{\mathbf{a}}(\underline{\theta}_l), \quad (5)$$

for $d = 1, \dots, D$, where the steering vector $\underline{\mathbf{a}}(\underline{\theta}_l)$ is

$$\underline{\mathbf{a}}(\underline{\theta}_l) = [1, e^{-j\pi \sin(\underline{\theta}_l)}, \dots, e^{-j\pi(N_t-1) \sin(\underline{\theta}_l)}]^T. \quad (6)$$

When the UE is located in the near-field region, $\underline{\mathbf{h}}_d$ is similar to the mmWave near-field one and thus will not be elaborated further here.

Using (5), the frequency-domain sub-6G channel at the k -th subcarrier $\underline{\mathbf{h}}_k \in \mathbb{C}^{N_t \times 1}$ is given by

$$\underline{\mathbf{h}}_k = \sum_{d=1}^D \underline{\mathbf{h}}_d e^{-j\frac{2\pi k}{K}d}, \quad (7)$$

for $k = 1, \dots, K$.

Through a fully digital receiver architecture in the sub-6G system, the frequency-domain channels at the K subcarriers can be estimated via sub-6G pilot transmission. To this end, the UE sends the uplink pilot signal $\underline{\mathbf{s}}_{p,k} = \sqrt{P_s/K}$ at the k -th subcarrier with P_s being the total power of the pilot signal. The received signals by the BS at the k -th subcarrier $\underline{\mathbf{y}}_{p,k}$ can be written as

$$\underline{\mathbf{y}}_{p,k} = \underline{\mathbf{h}}_k \underline{\mathbf{s}}_{p,k} + \underline{\mathbf{n}}_k, \quad (8)$$

where $\underline{\mathbf{n}}_k \sim \mathcal{CN}(0, \sigma_n^2 \mathbf{I}_{N_t})$ denotes the noise vector with σ_n^2 being the sub-6G noise power. The frequency-domain sub-6G channel estimate at the k -th subcarrier $\hat{\underline{\mathbf{h}}}_k$ can be obtained via a low-complexity least square (LS) algorithm, which is given by

$$\hat{\underline{\mathbf{h}}}_k = \underline{\mathbf{y}}_{p,k} \underline{\mathbf{s}}_{p,k}^{-1}. \quad (9)$$

We denote the frequency-domain sub-6G OFDM channel estimate as $\hat{\mathbf{H}} \triangleq [\hat{\underline{\mathbf{h}}}_1, \dots, \hat{\underline{\mathbf{h}}}_K]^H$.

C. Problem Formulation

Following prior works [10], [32], we consider the problem of beam selection from a predefined near-field codebook. Specifically, we adopt the polar codebook introduced in [9], denoted as $\mathcal{W} \triangleq (\mathbf{w}_{n,s})_{N_t \times S}$, where the numbers of candidate angles and distances are equal to the number of mmWave transmit antennas, N_t , and to an integer parameter S , respectively. Each codeword $\mathbf{w}_{n,s} = \mathbf{b}(\theta_n, r_{n,s})$ in the set \mathcal{W} corresponds to the (n, s) -th angle-distance sector, with

$$\begin{aligned} \theta_n &= \arcsin\left(\frac{-1 + 2n}{N_t}\right), \\ r_{n,s} &= \frac{(1 - \sin(\theta_n))^2 N_t^2 d^2}{2s\beta^2\lambda}, \end{aligned} \quad (10)$$

where β is the correlation parameter between neighboring codewords [9].

For a given mmWave channel sample \mathbf{H} , the *optimal beam* \mathbf{f}^* is defined as the codeword in set \mathcal{W} that maximizes the average spectral efficiency, i.e., as

$$\mathbf{f}^* = \mathbf{w}_{n^*,s^*} = \arg \max_{\mathbf{w}_{n,s} \in \mathcal{W}} R(\mathbf{w}_{n,s}, \mathbf{H}), \quad (11)$$

where the average spectral efficiency is given by

$$R(\mathbf{w}_{n,s}, \mathbf{H}) = \frac{1}{K} \sum_{k=1}^K \log_2 \left(1 + \frac{P_t}{K} \frac{|\mathbf{h}_k^H \mathbf{w}_{n,s}|^2}{\sigma_n^2} \right). \quad (12)$$

Most previous works [9]–[13] have focused on in-band beam training to determine the optimal near-field beam (11). However, these methods typically require a substantial number of pilots. As in [16], [19], [33], [34], we explore the potential of sub-6G information for near-field beam selection to reduce pilot overhead. Specifically, in order to account for the inherent uncertainty associated with the mapping from sub-6G information to mmWave beam selection, we propose to operate as follows:

- 1 **Sub-6G-based candidate beam selection:** Construct a candidate beam set $\mathcal{C}(\hat{\mathbf{H}})$ based on the sub-6G channel estimate $\hat{\mathbf{H}}$.
- 2 **MmWave beam training:** Perform limited mmWave beam training within the set $\mathcal{C}(\hat{\mathbf{H}})$ to choose a beam $\mathbf{f} = \mathbf{w}_{\hat{n},\hat{s}} \in \mathcal{C}(\hat{\mathbf{H}})$.

Traditional designs for candidate beam selection, such as top-K [16] and probability sum-based methods [34] lack theoretical guarantees on the quality of the pre-selected candidate beam set. Thus, the subsequent mmWave beam training may fail to return a well-performing beam in the codebook \mathcal{W} with a probability exceeding user's requirements.

To formalize theoretical guarantees for the candidate beam set, we first introduce a relaxed notion of beam optimality. To

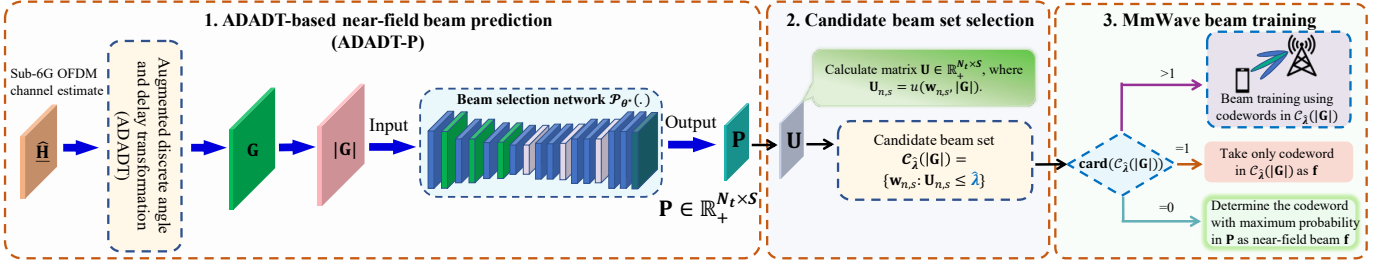


Fig. 3. The overall design of the SCAN-BEST framework.

this end, for any beam \mathbf{f} , we denote the *suboptimality ratio* as the ratio of the rate achieved by beam \mathbf{f} and the rate of the optimal beam \mathbf{f}^* , i.e.,

$$r(\mathbf{f}, \mathbf{H}) = \frac{R(\mathbf{f}, \mathbf{H})}{R(\mathbf{f}^*, \mathbf{H})}. \quad (13)$$

Then, a beam \mathbf{f} is said to be ϵ -suboptimal if it satisfies the condition

$$r(\mathbf{f}, \mathbf{H}) \geq 1 - \epsilon, \quad (14)$$

where ϵ , with $0 \leq \epsilon \leq 1$, is the suboptimality factor. In practice, the parameter ϵ is typically set in the range $0 \leq \epsilon \leq 0.2$, with $\epsilon = 0$ identifying the optimal beam \mathbf{f}^* .

In this paper, unlike prior studies [9], [10], [32], we aim to design a sub-6G information-aided solution that guarantees a user-specified probability $1 - \alpha \in [0, 1]$ of identifying an ϵ -suboptimal beam. Specifically, given a target suboptimality ratio ϵ , we wish to ensure that the probability of failing to obtain an ϵ -suboptimal beam is no larger than α , i.e.,

$$\Pr(r(\mathbf{f}, \mathbf{H}) < 1 - \epsilon) \leq \alpha. \quad (15)$$

Condition (15) is satisfied, for a well-designed mmWave training phase, as long as the probability that the candidate beam set $\mathcal{C}(\hat{\mathbf{H}})$ contains none codewords with suboptimality smaller than ϵ does not exceed α , i.e.,

$$\Pr(\nexists \mathbf{w} \in \mathcal{C}(\hat{\mathbf{H}}) : r(\mathbf{w}, \mathbf{H}) \leq 1 - \epsilon) \leq \alpha. \quad (16)$$

We will refer to the probability in (16) as the *miscoverage probability*.

III. SUB-6G CHANNEL AIDED NEAR-FIELD BEAM SELECTION FRAMEWORK

In this section, we first present an overview of SCAN-BEST, and then elaborate on its implementation.

A. Overview of SCAN-BEST

SCAN-BEST builds on deep learning for feature extraction [35] and on the statistical methodology of CRC [22]. For given suboptimal parameter ϵ and miscoverage probability α , SCAN-BEST, as illustrated in Fig. 3, proceeds along the following three stages:

- 1) **Augmented discrete angle and delay transformation-based near-field beam prediction (ADADT-P):** Structural information about multipath angles and distances is extracted from the raw sub-6G OFDM channel estimate $\hat{\mathbf{H}}$ using the augmented discrete angle and delay transformation (ADADT) [36]. The extracted features are used

as input to a deep learning model trained to assign each codeword in the codebook \mathcal{W} an estimated probability of being the optimal near-field beam [17].

- 2) **Sub-6G-based candidate beam set selection:** Using the predicted probabilities for all candidate codewords in \mathcal{W} , CRC is leveraged to select a near-field candidate beam subset $\mathcal{C}(\hat{\mathbf{H}})$ that ensures the desired target coverage rate condition in (16).
- 3) **MmWave beam training:** The near-field beam is determined by performing limited beam training only along the codeword within the candidate beam subset $\mathcal{C}(\hat{\mathbf{H}})$.

B. ADADT-based Near-Field Beam Prediction

In the first stage, we apply ADADT [36] to the sub-6G OFDM channel estimate $\hat{\mathbf{H}} \triangleq [\hat{\mathbf{h}}_1, \dots, \hat{\mathbf{h}}_K]$ for the purpose of extracting informative angle and delay attributes. These features are then used to predict the optimal beam in the codebook \mathcal{W} . Following [36], we introduce two oversampled discrete Fourier transform (DFT) matrices, $\mathbf{A} \in \mathbb{C}^{N_t \times N_t}$ and $\mathbf{V} \in \mathbb{C}^{K \times M}$ with $(M > K)$, which correspond to the angular DFT matrix and the temporal DFT matrix, respectively. Specifically, matrix \mathbf{A} is given by

$$\mathbf{A} = [\mathbf{a}(\phi_1), \dots, \mathbf{a}(\phi_{N_t})], \quad (17)$$

where $\phi_n = \arcsin(-1 + 2(n-1)/N_t)$, for all $n = 1, \dots, N_t$, and

$$\mathbf{a}(\phi_n) = \frac{1}{\sqrt{N_t}} [1, e^{j\pi \sin(\phi_n)}, \dots, e^{j\pi(N_t-1) \sin(\phi_n)}]^T. \quad (18)$$

Similarly, matrix \mathbf{V} is given by

$$\mathbf{V} = [\mathbf{v}(\zeta_1), \dots, \mathbf{v}(\zeta_M)], \quad (19)$$

where $\zeta_m = K(m-1)/(WM)$ for all $m = 1, 2, \dots, M$, and

$$\mathbf{v}(\zeta_m) = \frac{1}{\sqrt{K}} [1, e^{-j2\pi\zeta_m}, \dots, e^{-j2\pi\zeta_m(K-1)}]^T. \quad (20)$$

With these matrices, we decompose the channel estimate $\hat{\mathbf{H}}$ as

$$\mathbf{G} = \mathbf{A}^H \hat{\mathbf{H}} \mathbf{V}, \quad (21)$$

where $\mathbf{G} \in \mathbb{C}^{N_t \times M}$ represents the augmented discrete angle and delay profile of $\hat{\mathbf{H}}$.

As illustrated in Fig. 1a, each element in \mathbf{G} corresponds to the gain of an individual angle-delay bin, indicating the likelihood of a strong path's presence in the given bin [15]. Accordingly, the angle, distance, and energy information of paths are mainly contained in the absolute values of the elements of \mathbf{G} . Therefore, we adopt for beam prediction the

features given by the entry-wise absolute value of matrix \mathbf{G} , i.e., $|\mathbf{G}|$.

A neural network is introduced to map the input matrix $|\mathbf{G}|$ to a probability matrix $\mathbf{P} \in [0, 1]^{N_t \times S}$, where the entry $\mathbf{P}_{n,s}$ represents the predicted probability that the codeword $\mathbf{w}_{n,s}$ is the optimal near-field beam. As depicted in Fig. 3, the mapping between matrices $|\mathbf{G}|$ and \mathbf{P} , denoted as $\mathbf{P} = \mathcal{P}_{\boldsymbol{\theta}}(|\mathbf{G}|)$, is parameterized with a vector $\boldsymbol{\theta}$, and constructed using 2D CNN blocks. The 2D CNN blocks are arranged sequentially, with each block consisting of Conv2D, BatchNorm2D, ReLU, and MaxPool2D layers. Moreover, to ensure that the network's output forms a valid probability matrix, a softmax activation function is applied in the last layer of the network.

In order to train the neural network mapping $\mathbf{P} = \mathcal{P}_{\boldsymbol{\theta}}(|\mathbf{G}|)$, we assume the availability of a dataset $\mathcal{D}_{\text{tr}} \triangleq \{|\mathbf{G}_i|, n_i^*, s_i^*\}_{i=1}^{N_{\text{tr}}}$ associating a feature matrix $|\mathbf{G}_i|$ with the corresponding index (n_i^*, s_i^*) of the optimal beam in (11). Training is done by minimizing the standard cross-entropy loss, yielding the optimized parameter

$$\boldsymbol{\theta}^* = \arg \max_{\boldsymbol{\theta}} \left\{ - \sum_{i=1}^{N_{\text{tr}}} \log \mathcal{P}_{\boldsymbol{\theta}, n_i^*, s_i^*}(|\mathbf{G}_i|) \right\}, \quad (22)$$

where $\mathcal{P}_{\boldsymbol{\theta}, n_i^*, s_i^*}(|\mathbf{G}_i|)$ is the (n_i^*, s_i^*) -th entry of matrix $\mathcal{P}_{\boldsymbol{\theta}}(|\mathbf{G}_i|)$.

C. Sub-6G-based Candidate Beam Set Selection

Given the trained model $\mathcal{P}_{\boldsymbol{\theta}^*}(\cdot)$ in (22), and given an input $|\mathbf{G}|$, SCAN-BEST evaluate a negatively oriented score for codeword $\mathbf{w}_{n,s}$, namely

$$u(n, s, |\mathbf{G}|) = -\log P_{\max}(|\mathbf{G}|) - \log \mathbf{P}_{n,s}(|\mathbf{G}|), \quad (23)$$

where $P_{\max}(|\mathbf{G}|) = \max_{n,s \in N_t \times S} \mathbf{P}_{n,s}(|\mathbf{G}|)$ and $\mathbf{P}_{n,s}(|\mathbf{G}|) = \mathcal{P}_{\boldsymbol{\theta}^*}(|\mathbf{G}|)_{n,s}$. The term $-\log P_{\max}(|\mathbf{G}|)$ is referred to as the Rényi min-entropy for the predictive conditional probability $\mathcal{P}_{\boldsymbol{\theta}^*}(|\mathbf{G}|)$, which provide a measure of the uncertainty of the model $\mathcal{P}_{\boldsymbol{\theta}^*}(\cdot)$ regarding this prediction with input $|\mathbf{G}|$ [37]. Adding this term to the negative log-likelihood $-\log \mathbf{P}_{n,s}(|\mathbf{G}|)$ degrades the score $u(n, s, |\mathbf{G}|)$ when the predictive uncertainty is high. Recall, in fact, that a smaller value of the score $u(n, s, |\mathbf{G}|)$ indicates that the codeword $\mathbf{w}_{n,s}$ is predicted to be more likely to be optimal.

The subset $\mathcal{C}_{\lambda}(|\mathbf{G}|)$ of candidate beams includes all codewords in set \mathcal{W} whose scores (23) are no larger than a threshold λ , i.e.,

$$\mathcal{C}_{\lambda}(|\mathbf{G}|) = \{\mathbf{w}_{n,s} \in \mathcal{W} : u(n, s, |\mathbf{G}|) \leq \lambda\}. \quad (24)$$

In order to select the threshold λ so that the coverage condition (16) is satisfied, we adopt CRC [22]. To this end, we assume a held-out calibration dataset $\mathcal{D}_{\text{cal}} \triangleq \{\hat{\mathbf{H}}_i, \mathbf{H}_i\}_{i=1}^{N_{\text{cal}}}$, where $\hat{\mathbf{H}}_i$ is the sub-6G channel estimate and \mathbf{H}_i is a corresponding ground-truth mmWave channel. Using the calibration dataset, the probability (16) is estimated, and the estimate is evaluated as a function of the threshold λ . This evaluation is leveraged to find a threshold that satisfies the inequality (16).

Specifically, using the channel estimate $\hat{\mathbf{H}}_i$, the corresponding \mathbf{G}_i is obtained using (21). Then, the set $\mathcal{C}_{\lambda}(|\mathbf{G}_i|)$ is evaluated using (24) for all calibration data points $i = 1, \dots, N_{\text{cal}}$.

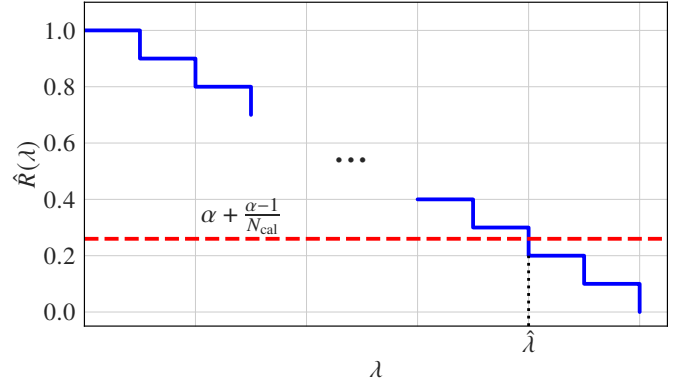


Fig. 4. A simple illustration of $\hat{R}(\lambda)$ (blue line), the orange line denotes the desired risk level.

Finally, the miscoverage probability (16) is estimated using the calibration data set as

$$\hat{R}(\lambda) = \frac{1}{N_{\text{cal}}} \sum_{i=1}^{N_{\text{cal}}} \mathbf{1}(\nexists \mathbf{w} \in \mathcal{C}_{\lambda}(|\mathbf{G}_i|) : r(\mathbf{w}, \mathbf{H}_i) \geq 1 - \epsilon). \quad (25)$$

Proposition 1. The subset $\mathcal{C}_{\hat{\lambda}}(|\mathbf{G}|)$ in (24) with the threshold

$$\hat{\lambda} = \inf \left\{ \lambda \in \mathbb{R} : \hat{R}(\lambda) \leq \alpha + \frac{\alpha - 1}{N_{\text{cal}}} \right\} \quad (26)$$

attains the target coverage rate $1 - \alpha$ in (16) for any input $|\mathbf{G}|$ and any predictive model $\mathcal{P}_{\boldsymbol{\theta}^*}(\cdot)$.

Accordingly, as illustrated in Fig. 4, the threshold is selected so that the miscoverage probability (25) satisfies the condition (16) with the caveat that the reliability requirement is made stricter—from α to $\alpha + (\alpha - 1)/N_{\text{cal}}$. Note that the added term in the coverage probability α decreases to zero as $N_{\text{cal}} \rightarrow \infty$.

Finding the threshold (26) is computationally straightforward given that the empirical risk $\hat{R}(\lambda)$ is monotonically non-increasing relative to λ (see Fig. 4). Furthermore, a threshold satisfying the condition (26) always exists, since the choice $\lambda = \max_{i \in \{1, \dots, N_{\text{cal}}\}} u(n_i^*, s_i^*, |\mathbf{G}_i|)$ yields $\hat{R}(\lambda) = 0$. Following the properties of CRC [22], this choice of the threshold ensures the condition (16).

D. MmWave Beam Training

For a given input $|\mathbf{G}|$, the candidate beam set $\mathcal{C}_{\hat{\lambda}}(|\mathbf{G}|)$ may have any cardinality between zero and $N_t S$. Accordingly, the mmWave training stage operates as follows:

- 1) If the set $\mathcal{C}_{\hat{\lambda}}(|\mathbf{G}|)$ is empty, SCAN-BEST selects the most likely codeword corresponding to the maximum probability in \mathbf{P} as the final beam \mathbf{f} .
- 2) If the set $\mathcal{C}_{\hat{\lambda}}(|\mathbf{G}|)$ has cardinality equal to 1, the only codeword in $\mathcal{C}_{\hat{\lambda}}(|\mathbf{G}|)$ is selected as the final beam \mathbf{f} .
- 3) If the set $\mathcal{C}_{\hat{\lambda}}(|\mathbf{G}|)$ has cardinality larger than 1, mmWave beam training is performed to select final beam \mathbf{f} .

MmWave training leverages the transmission of pilot symbols in the uplink of the mmWave band. To elaborate, let $s_{p,k} = \sqrt{P_s/K}$ denote the uplink pilot signal at the k -th subcarrier, where P_s represents the total power allocated for pilot transmission. When employing the codeword \mathbf{w} , the

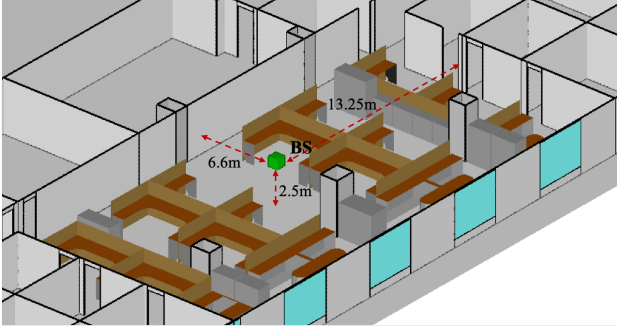


Fig. 5. An illustration of simulation setup.

corresponding received signal at the k -th subcarrier, denoted as $y_{\mathbf{w},k}$, is given by:

$$y_{\mathbf{w},k} = \mathbf{w}^T \mathbf{h}_k s_{p,k} + \mathbf{w}^T \mathbf{n}_k, \quad (27)$$

where $\mathbf{n}_k \sim \mathcal{CN}(\mathbf{0}, \sigma_n^2 \mathbf{I}_{N_t})$ denotes the noise vector with variance σ_n^2 . Based on the received signal (27), the final beam \mathbf{f} is selected as the codeword corresponding to the maximum received power:

$$\mathbf{f} = \arg \max_{\mathbf{w} \in \mathcal{C}_{\hat{\lambda}}(|\mathbf{G}|)} \sum_{k=1}^K |y_{\mathbf{w},k}|^2. \quad (28)$$

If more pilots are transmitted per beam, the average power is computed in (28).

The entire implementation of SCAN-BEST framework is summarized in Algorithm 1.

Algorithm 1 SCAN-BEST

- Input:** Sub-6G OFDM channel estimates $\hat{\mathbf{H}}$, target miscoverage rate α
- Output:** Near-field beam \mathbf{f}
- 1: Convert $\hat{\mathbf{H}}$ into its ADADT form \mathbf{G} using (21)
 - 2: Produce the ADADT-P near-field beam probability matrix $\mathcal{P}_{\theta^*}(|\mathbf{G}|)$
 - 3: Construct near-field candidate beam set $\mathcal{C}_{\hat{\lambda}}(|\mathbf{G}|)$ via (24)
 - 4: **if** $\mathcal{C}_{\hat{\lambda}}(|\mathbf{G}|)$ is empty, i.e., $\text{card}(\mathcal{C}_{\hat{\lambda}}(|\mathbf{G}|)) = 0$ **then**
 - 5: Identify the codeword with the largest probability in $\mathbf{P} = \mathcal{P}_{\theta^*}$ as the near-field beam \mathbf{f}
 - 6: **else if** $\text{card}(\mathcal{C}_{\hat{\lambda}}(|\mathbf{G}|)) = 1$ **then**
 - 7: Assign the only codeword in $\mathcal{C}_{\hat{\lambda}}(|\mathbf{G}|)$ as \mathbf{f}
 - 8: **else**
 - 9: Conduct uplink beam training using the codewords in $\mathcal{C}_{\hat{\lambda}}(|\mathbf{G}|)$ and then select the codeword with the strongest received signal power as \mathbf{f} using (28)
 - 10: **end if**

IV. NUMERICAL RESULTS

In this section, we present experimental results to validate the performance of SCAN-BEST.

A. Simulation Scenario and System Parameter Setup

As depicted in Fig. 5, we consider an indoor scenario within an area of dimensions 13.2 m \times 26.5 m. The BS with height 2.5 m, is located at the center of the area. The UE is randomly placed within the area, with a height of 1 m. The UE is assumed to be the height of 1 m, and it can be located

TABLE I
SYSTEM PARAMETERS

Notations	Parameters	Values
f_c, f_c	Operating frequency of mmWave, sub-6G system (GHz)	73, 3.5
W, W	Bandwidth of mmWave, sub-6G system (MHz)	200, 80
K, K	Number of subcarriers of mmWave, sub-6G system	64, 32
N_t, N_t	Number of mmWave, sub-6G antennas at the BS	256, 16
P_t, P_s	Total power of mmWave downlink, uplink pilot (dBm)	25, 25
P_s	Power of sub-6G pilot signals (dBm)	10
σ_n^2, σ_n^2	Noise power of mmWave, sub-6G system (dBm)	$-173.8 + 90 + 10 \log_{10}(W)$ $-173.8 + 90 + 10 \log_{10}(W)$
S, β	Number of candidate distances and correlation parameter of \mathcal{W}	7, 1.6

TABLE II
NETWORK PARAMETERS

Input/Output Channel	Layers	Convolution Kernels
(1, 32)	{Conv2D, BatchNorm2D, ReLU} \times 2, MaxPool2D	(8, 4)
(32, 64)	idem	(5, 3)
(64, 128)	idem	(5, 3)
(128, 256)	idem	(5, 3)
(256, 256)	Conv2D, BatchNorm2D	(3, 3)
(256, 128)	Upsample, Conv2D, BatchNorm2D, ReLU Conv2D, BatchNorm2D	(3, 3)
(128, 64)	idem	(7, 3)
(64, 32)	idem	(7, 3)
(32, 16)	idem	(7, 3)
(16, 8)	idem	(7, 3)
(8, 1)	Conv2D	(7, 3)
/	Flatten, Softmax, Reshape	/

anywhere within the room, leading to the LoS condition or NLoS conditions. More detailed system parameters are listed in Table I, with exceptions marked explicitly in the text.

We first collect a total of 10,000 samples from the above indoor scenario via a ray-tracing software [14], each of which consists of a pair of sub-6G channel estimate and true mmWave channel $\{\hat{\mathbf{H}}, \mathbf{H}\}$. These samples are randomly split for training, validating, calibration, and testing, respectively, with the ratio of 50%, 10%, 20%, and 20%, respectively. The network $\mathcal{P}_{\theta}(\cdot)$ is set up using the parameters provided in Table II, and is trained using the Adam optimizer with a batch size of 128, an initial learning rate of 0.0002, and the learning rate scheduler ‘‘ReduceLROnPlateau’’ [38]. This scheduler automatically reduces the learning rate when the model’s performance on the validation set ceases to improve or demonstrates only marginal improvements over a specified number of training epochs. The maximum training epoch is set to 200, and, to prevent overfitting, a classical early stopping criterion is adopted, which stops the training process if the validation loss does not improve for a certain number of epochs.

TABLE III
BASELINE METHODS

Method Category	Method	Predictive Model	Candidate Beam Subset	MmWave Beam Training
MmWave-based baselines	EBS [10]	✗	✗	Exhaustive search with $N_t S$ pilots Two-stage search with $N_t + 3S$ pilots
	FNBS [10]	✗	✗	
Sub 6GHz-based baselines	SPBS + Top-K	SPBS	Top-K	Limited mmWave beam training within candidate beam set
	SPBS + PS	SPBS	PS	
	SPBS + CRC	SPBS	CRC	
	ADADT-P + Top-K	ADADT-P	Top-K	
	ADADT-P + PS	ADADT-P	PS	
Our method	SCAN-BEST	ADADT-P	CRC	

B. Performance Metrics and Baselines

To comprehensively assess the overall performance of proposed SCAN-BEST, we evaluate the following performance metrics:

- **Achieved coverage rate:** the complement of the probability (15), quantifying the probability that a codeword in $\mathcal{C}_{\hat{\lambda}}(|\mathbf{G}|)$ satisfies the condition in (14) over the testing dataset;
- **Average suboptimality ratio:** the average suboptimality ratio (14) evaluated over the testing dataset.

As benchmarks, we consider two classical methods to select the candidate beam subset based the given predictive model.

- **Top-K selection [16]:** Identify the K codewords with the highest predictive probabilities to form the candidate beam set.
- **Probability sum (PS) selection [34]:** Choose the smallest set of codewords whose cumulative predictive probability exceeds a predefined threshold (set to 0.99 unless otherwise specified) to form the candidate beam set.

Specifically, we analyze the performance of mmWave and sub 6GHz-based baselines listed in Table III. These include different combination of predictive model and beam selection scheme. One of the considered predictors is the proposed ADADT-P, while the other is an adaptation of the method from [33] for the single-user scenario. This method, denoted as SPBS, employs a neural network to predict the optimal near-field beam probabilities directly from sub-6G pilot signals. Furthermore, we evaluate the following schemes that do not leverage sub-6G information:

- **Exhaustive beam search (EBS) [10]:** This scheme conducts the beam training across all codewords in the near-field polar-domain codebook \mathcal{W} , requiring $N_t \times S$ mmWave pilots.
- **Fast near-field beam search (FNBS) [10]:** This scheme first performs angle-domain beam sweeping to identify high-gain angle indices and then uses the polar-domain codebook to sweep the distance range corresponding to the selected angles.

C. Coverage Rate Guarantee of SCAN-BEST

To start, we evaluate the reliability guarantees provided by SCAN-BEST in term of coverage rate (16). Fig. 6 presents the achieved coverage rates, along with the sizes of the

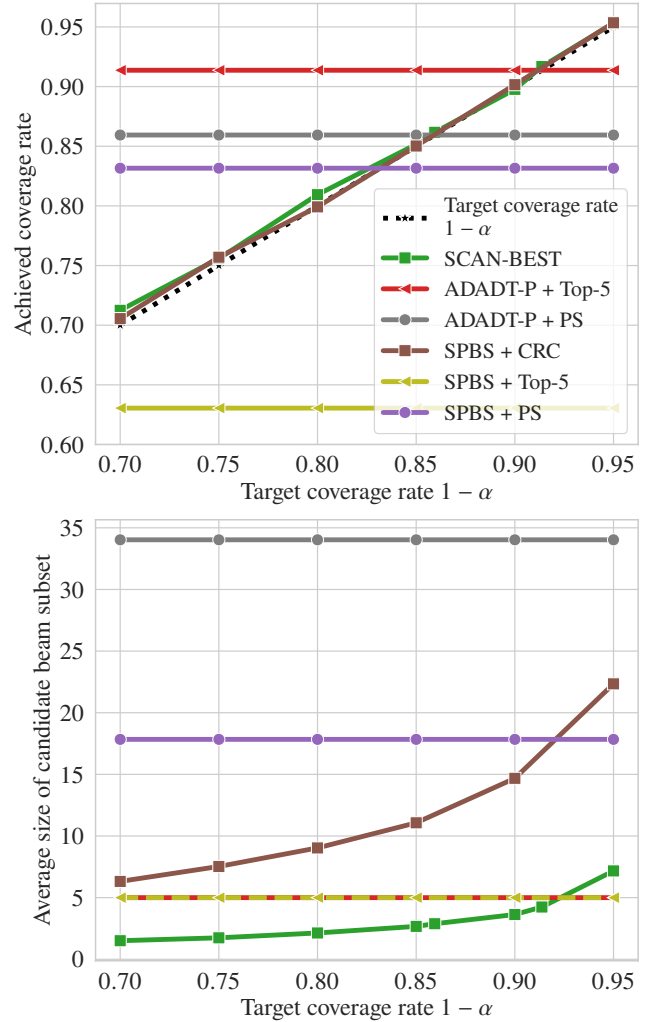


Fig. 6. Achieved coverage rates and average sizes of candidate beam subset of SCAN-BEST and baselines for $\epsilon = 0.15$.

candidate beam subsets for SCAN-BEST and for sub 6GHz-based baselines when the suboptimality target is $\epsilon = 0.15$. For results with other values of ϵ , refer to Fig. 11 in Appendix A. Confirming the theory [Proposition 1], with the help of CRC, both SCAN-BEST and SPBS + CRC, combining the SPBS prediction and CRC, can achieve the target coverage rate by dynamically increasing the size of candidate beam subset. Thanks to the more use of a more effective predictor, ADADT-

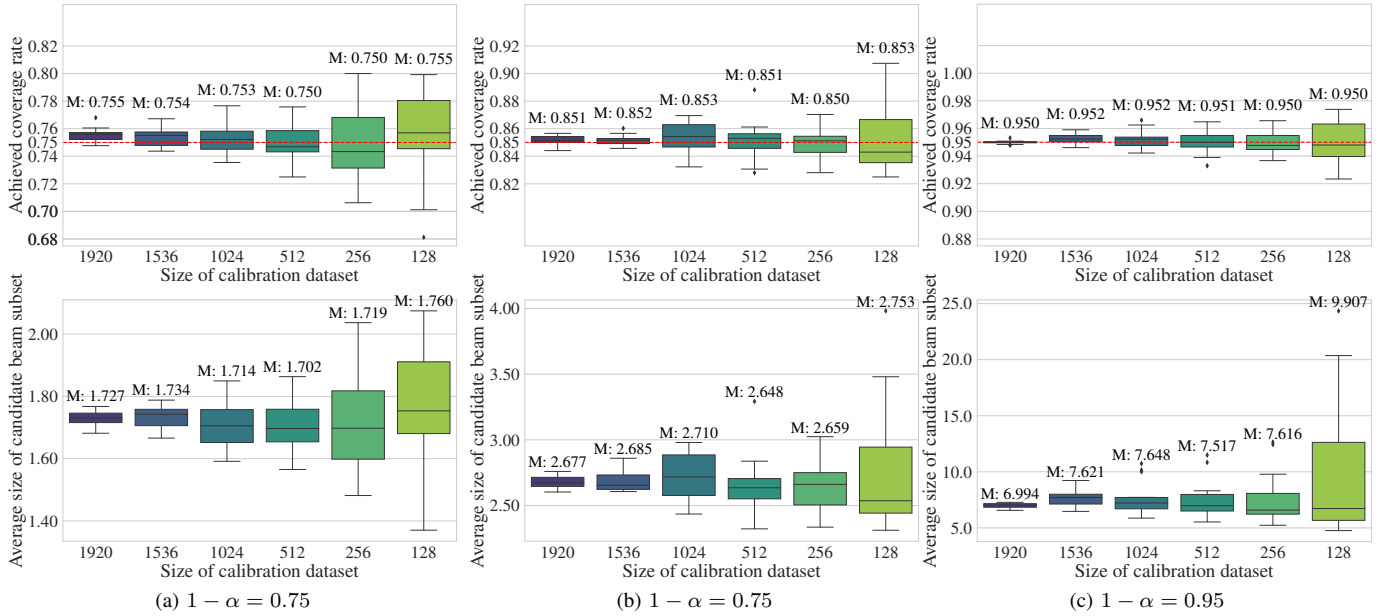


Fig. 7. Box plots for the achieved coverage rate and the size of the candidate beam subset under different calibration dataset sizes, with target coverage rates $1 - \alpha$ of (a) 0.75, (b) 0.85, and (c) 0.95. The red lines denote the target coverage rates $1 - \alpha$, while “M” indicates the mean.

P, SCAN-BEST requires a smaller candidate beam subset as compared to SPBS + CRC to achieve the same coverage rate.

In contrast, the baselines using candidate beam subsets constructed via Top-K or PS achieve only fixed coverage rates, as their candidate beam subsets cannot be dynamically adjusted to meet specific target coverage rates. Furthermore, when achieving the same coverage rate as ADADT-P + Top-5 and ADADT-P + PS, SCAN-BEST attains smaller candidate beam subsets. Specifically, the average sizes of the candidate beam subsets for ADADT-P + Top-5 and ADADT-P + PS=0.99 are 5 and 33.9 for $\alpha = 0.086$ and $\alpha = 0.106$, respectively, while those for SCAN-BEST are 4.2 and 2.8, respectively.

D. Impact of the Size of Calibration Dataset

Here, we analyze the achieved coverage rate and candidate beam subset size when varying the calibration dataset sizes. Fixing the suboptimality parameter $\epsilon = 0.15$ and the target coverage rates $1 - \alpha = 0.75, 0.85, 0.95$, and taking SCAN-BEST as an example, Fig. 7 presents key statistical characteristics of the achieved coverage rate and candidate beam subset size for different calibration dataset sizes. The box plots, showing median (horizontal line), first inter-quartile intervals (box), and support (whiskers) are evaluated with 15 independent experiments. The results show that, regardless of the dataset size, the average achieved coverage rate remains above the target coverage rate. Larger dataset sizes offer more reliable guarantees for the coverage rate and a more stable size of the candidate beam subset. Finally, higher target coverage rates generally demand smaller calibration datasets. For instance, for the same calibration dataset size N_{cal} , the inter-quartile ranges of achieved coverage rates at $1 - \alpha = 0.95$ are narrower than those at $1 - \alpha = 0.75$ and $1 - \alpha = 0.85$.

E. Comparison with MmWave-based Methods

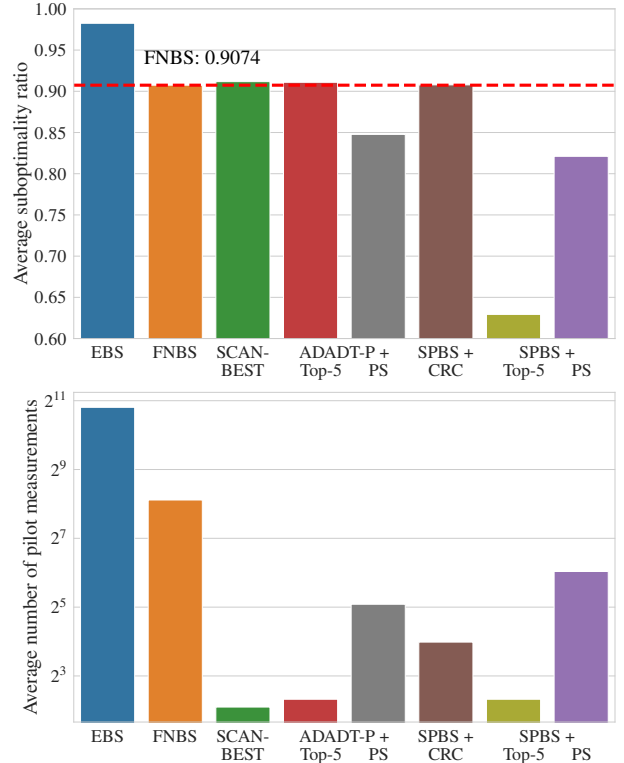


Fig. 8. Comparison of the average suboptimality ratio and of the number of pilot symbols for SACN-BEST, mmWave-based, and sub 6GHz-based baselines.

Fig. 8 compares the average suboptimality ratio and the number of pilot symbols of SACN-BEST, mmWave-based, and sub 6GHz-based baselines. Given the average suboptimality

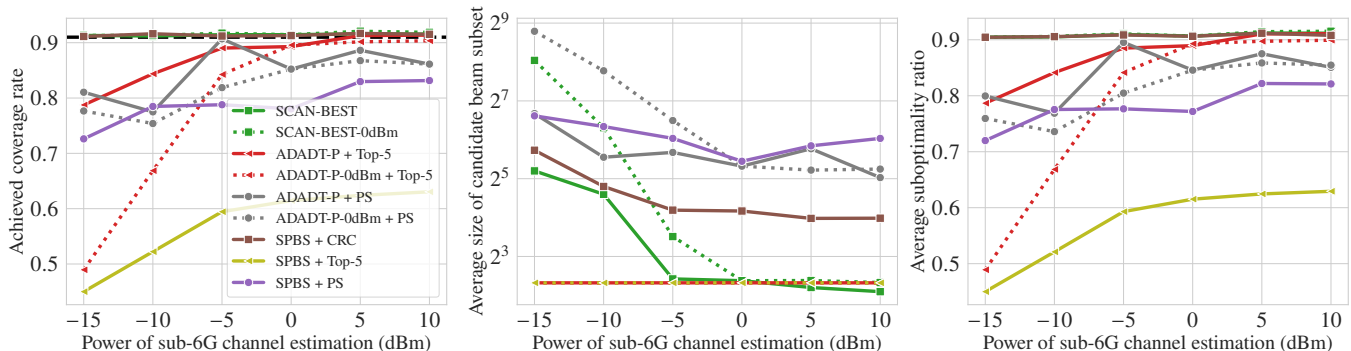


Fig. 9. Achieved coverage rates, average sizes of candidate beam subset, and average suboptimality ratios for SCAN-BEST and baselines under different numbers of sub-6G antennas.

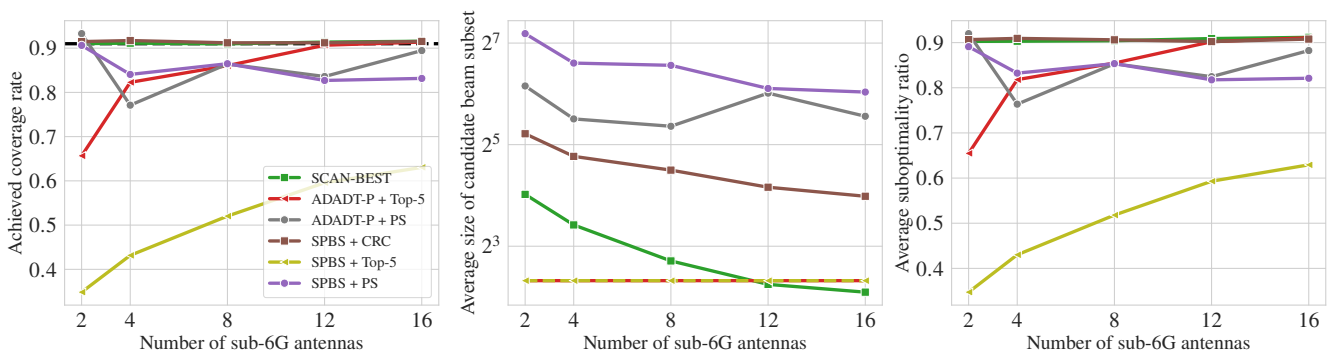


Fig. 10. Achieved coverage rates, average sizes of candidate beam subset, and average suboptimality ratios for SCAN-BEST and baselines under different powers of sub-6G channel estimation.

ratio of FNBS (0.9074), we set the target coverage rate of SCAN-BEST and SPBS + CRC as $1 - \alpha = 0.91$. SCAN-BEST, ADADT-P + Top-5, and SPBS + CRC achieve the higher average suboptimality ratio than FNBS while using only an average of 4.2, 5, and 15.8 mmWave pilots, respectively. Moreover, the lower mmWave pilot consumption of SCAN-BEST compared to ADADT-P + Top-5 and SPBS + CRC further demonstrates the efficiency of the combination of ADADT-P and CRC.

F. Impact of Sub-6G System Parameters

1) *Impact of Sub-6G Channel Estimation Power:* Following the previous setting of $1 - \alpha = 0.91$ and $\epsilon = 0.15$, we investigate the impact of the sub-6G channel estimation power, P_s , on the performance of SCAN-BEST. Fig. 9 shows that both SCAN-BEST and SPBS + CRC reliably maintain coverage rate guarantee $1 - \alpha = 0.91$, regardless of the power P_s . When P_s decreases, the candidate beam subset dynamically expands to satisfy the target coverage rate. Furthermore, we assess the generalization capability of SCAN-BEST by applying ADADT-P trained at $P_s = 0$ dBm, denoted by “SCAN-BEST-0dBm”, to test on datasets characterized by different power P_s . SCAN-BEST-0dBm exhibits similar performance to SCAN-BEST, which is attributed to the fact that CRC is a model-free calibration approach. In contrast, baselines using the Top-K and PS candidate beam subsets inevitably experience performance degradation or fluctuation as the power P_s varies.

2) *Impact of the Number of Sub-6G Antennas:* Similarly, under the setting of $1 - \alpha = 0.91$ and $\epsilon = 0.15$, SCAN-BEST and SPBS + CRC provides a reliable coverage rate guarantee of 0.91, regardless of the number of antennas N_t , as shown in Fig. 10. In scenarios with low number of antennas N_t , which leads to poor angle resolution, both SCAN-BEST and SPBS + CRC dynamically expand their candidate beam subsets. However, SCAN-BEST maintains smaller candidate beam subsets due to the efficiency of ADADT-P.

V. CONCLUSION

In this paper, we propose SCAN-BEST, a novel theoretically principled framework to enhance near-field beam selection while ensuring a guaranteed coverage rate. The framework employs a 2D CNN to exploit the spatial-temporal congruence between sub-6G and mmWave channels, enabling the prediction of the optimal near-field beam probabilities from sub-6G ADADT data. A novel CRC-based module constructs a near-field candidate beam set with formal optimality guarantees, which is refined through mmWave beam training to determine the final near-field beam. Extensive numerical evaluations demonstrate the effectiveness of SCAN-BEST in ensuring statistical suboptimality performance level. The proposed framework also achieves reliable calibration across various target coverage rates. Furthermore, SCAN-BEST exhibits excellent scalability and robustness across diverse sub-6G system parameters. Future work may focus on leveraging

CRC to develop reliable beamforming schemes for multi-user dual-band systems and multi-modality-aided scenarios.

APPENDIX A
PROOF OF PROPOSITION 1

Given the pretrained distribution $\mathcal{P}_{\theta^*}(|\mathbf{G}|)$ and the definition of the candidate beam subset $\mathcal{C}_\lambda(|\mathbf{G}|)$ in (24), where \mathbf{G} is obtained from $\hat{\mathbf{H}}$ via (21), the miscorverage probability requirement in (16) can be expressed as

$$\Pr(\nexists \mathbf{w} \in \mathcal{C}_\lambda(|\mathbf{G}|) : r(\mathbf{w}, \mathbf{H}) \geq 1 - \epsilon) \leq \alpha, \quad (29)$$

where the probability is taken over the underlying distribution of $\{\hat{\mathbf{H}}, \mathbf{H}\}$.

We define a loss function $\ell(\hat{\mathbf{H}}, \mathbf{H}, \lambda) \in \{0, 1\}$ as

$$\ell(\hat{\mathbf{H}}, \mathbf{H}, \lambda) = \mathbb{1}(\nexists \mathbf{w} \in \mathcal{C}_\lambda(|\mathbf{G}|) : r(\mathbf{w}, \mathbf{H}) \geq 1 - \epsilon). \quad (30)$$

As a result, the miscorverage probability requirement in (16) is equivalent to

$$\Pr(\ell(\hat{\mathbf{H}}, \mathbf{H}, \lambda) = 1) \leq \alpha, \quad (31)$$

which can be expressed as

$$\mathbb{E}[\ell(\hat{\mathbf{H}}, \mathbf{H}, \lambda)] \leq \alpha. \quad (32)$$

Thus, the miscorverage probability requirement in (16) is equivalent to the risk control problem in (32).

The empirical risk function $\hat{R}(\lambda)$ in (25) can be written as

$$\hat{R}(\lambda) = \frac{1}{N_{\text{cal}}} \sum_{i=1}^{N_{\text{cal}}} \ell(\hat{\mathbf{H}}_i, \mathbf{H}_i, \lambda). \quad (33)$$

With a little abuse of notation, we denote $\ell(\hat{\mathbf{H}}_i, \mathbf{H}_i, \lambda)$ as $\ell_i(\lambda)$, hence $\hat{R}(\lambda)$ can be expressed as $\hat{R}(\lambda) = \sum_{i=1}^{N_{\text{cal}}} \ell_i(\lambda) / N_{\text{cal}}$. Here, we introduce an auxiliary risk function $\hat{R}_f(\lambda)$ accounting for both calibration samples $\{\hat{\mathbf{H}}_i, \mathbf{H}_i\}_{i=1}^{N_{\text{cal}}}$ and a future sample $\{\hat{\mathbf{H}}_{N_{\text{cal}}+1}, \mathbf{H}_{N_{\text{cal}}+1}\}$, which is given by

$$\hat{R}_f(\lambda) = \frac{1}{N_{\text{cal}} + 1} \sum_{i=1}^{N_{\text{cal}}+1} \ell_i(\lambda). \quad (34)$$

Proposition 2. *The functions $\ell_i(\lambda)$ is monotonically non-increasing w.r.t. λ .*

Proof. For an arbitrary pair $\{\hat{\mathbf{H}}_i, \mathbf{H}_i\}$, assume $\lambda_1 < \lambda_2$, and consider two candidate beam sets $\mathcal{C}_{\lambda_1}(|\mathbf{G}_i|) = \{\mathbf{w}_{n,s} \in \mathcal{W} : u(n, s, |\mathbf{G}_i|) \leq \lambda_1\}$ and $\mathcal{C}_{\lambda_2}(|\mathbf{G}_i|) = \{\mathbf{w}_{n,s} \in \mathcal{W} : u(n, s, |\mathbf{G}_i|) \leq \lambda_2\}$. For any $\mathbf{w}_{n,s} \in \mathcal{C}_{\lambda_1}(|\mathbf{G}_i|)$, it follows $u(n, s, |\mathbf{G}_i|) \leq \lambda_1 \leq \lambda_2$, which implies $\mathbf{w}_{n,s} \in \mathcal{C}_{\lambda_2}(|\mathbf{G}_i|)$. Hence, we have the implication

$$\lambda_1 < \lambda_2 \implies \mathcal{C}_{\lambda_1}(|\mathbf{G}_i|) \subset \mathcal{C}_{\lambda_2}(|\mathbf{G}_i|).$$

It can be also seen that the inequality $\ell_i(\lambda_1) \geq \ell_i(\lambda_2)$ holds. \square

We also have

$$\begin{aligned} \hat{R}_f(\lambda) &= \frac{N_{\text{cal}}}{N_{\text{cal}} + 1} \hat{R}(\lambda) + \frac{\ell_{N_{\text{cal}}+1}(\lambda)}{N_{\text{cal}} + 1} \\ &\stackrel{(a)}{\leq} \frac{N_{\text{cal}}}{N_{\text{cal}} + 1} \hat{R}(\lambda) + \frac{1}{N_{\text{cal}} + 1}, \end{aligned} \quad (35)$$

where condition (a) holds because $\ell_{N_{\text{cal}}+1}(\lambda) \in \{0, 1\} \leq 1$. Then, using the optimized $\hat{\lambda}$ in (26), we obtain that

$$\frac{N_{\text{cal}}}{N_{\text{cal}} + 1} \hat{R}(\hat{\lambda}) + \frac{1}{N_{\text{cal}} + 1} \leq \alpha. \quad (36)$$

According to the inequality in (35), this implies that

$$\begin{aligned} \hat{R}_f(\hat{\lambda}) &\leq \frac{N_{\text{cal}}}{N_{\text{cal}}+1} \hat{R}(\hat{\lambda}) + \frac{1}{N_{\text{cal}}+1} \leq \alpha, \\ &\quad \downarrow \\ \hat{R}_f(\hat{\lambda}) &\leq \alpha. \end{aligned} \quad (37)$$

Introducing $\hat{\lambda}' = \inf\{\lambda \in \mathbb{R} : \hat{R}_f(\lambda) \leq \alpha\}$, we know that $\hat{\lambda}' \leq \hat{\lambda}$. Thus, according to Proposition 2, we obtain

$$\mathbb{E}[\ell_{N_{\text{cal}}+1}(\hat{\lambda})] \leq \mathbb{E}[\ell_{N_{\text{cal}}+1}(\hat{\lambda}')]. \quad (38)$$

In mathematics, a bag (also called a multiset) is a collection where elements can appear more than once.

Lemma 1 (From [39]). *If the random variables x_1, \dots, x_n, x_{n+1} are exchangeable, and conditioned on the bag of realization of $\{x_1, \dots, x_n, x_{n+1}\}$, the random variable x_{n+1} is uniformly distributed in the set $\{x_1, \dots, x_n, x_{n+1}\}$.*

Since the calibration samples $\{\hat{\mathbf{H}}_i, \mathbf{H}_i\}_{i=1}^{N_{\text{cal}}}$ and the future sample $\{\hat{\mathbf{H}}_{N_{\text{cal}}+1}, \mathbf{H}_{N_{\text{cal}}+1}\}$ are i.i.d. from the same scenario, they are exchangeable. According to the exchangeability-preserving theorem (Theorem 3 in [21]), the functions $\ell_1(\lambda), \dots, \ell_{N_{\text{cal}}}(\lambda), \ell_{N_{\text{cal}}+1}(\lambda)$ are also exchangeable, and we obtain

$$\ell_{N_{\text{cal}}+1}(\lambda) \sim \text{Uniform}(\ell_1(\lambda), \dots, \ell_{N_{\text{cal}}}(\lambda), \ell_{N_{\text{cal}}+1}(\lambda)). \quad (39)$$

Conditioned on the bag of realization of $\{\ell_1(\lambda), \dots, \ell_{N_{\text{cal}}}(\lambda), \ell_{N_{\text{cal}}+1}(\lambda)\}$, when $\lambda = \hat{\lambda}'$, we have

$$\mathbb{E}[\ell_{N_{\text{cal}}+1}(\hat{\lambda}')] = \frac{1}{N_{\text{cal}}+1} \sum_{i=1}^{N_{\text{cal}}+1} \ell_i(\hat{\lambda}') = \hat{R}_f(\hat{\lambda}') \stackrel{(b)}{\leq} \alpha, \quad (40)$$

$$\downarrow \\ \mathbb{E}[\ell_{N_{\text{cal}}+1}(\hat{\lambda}')] \leq \alpha,$$

where the condition (b) holds according to the definition of $\hat{\lambda}'$. Finally, according to (38), we obtain the following result:

$$\mathbb{E}[\ell_{N_{\text{cal}}+1}(\hat{\lambda})] \leq \alpha. \quad (41)$$

REFERENCES

- [1] C. Liu, M. Li, S. V. Hanly, P. Whiting, and I. B. Collings, "Millimeter-wave small cells: Base station discovery, beam alignment, and system design challenges," *IEEE Wireless Communications*, vol. 25, no. 4, pp. 40–46, 2018.
- [2] Y. Liu, C. Ouyang, Z. Ding, and R. Schober, "The road to next-generation multiple access: A 50-year tutorial review," *Proceedings of the IEEE*, vol. 112, no. 9, pp. 1100–1148, 2024.
- [3] M. Cui, Z. Wu, Y. Lu, X. Wei, and L. Dai, "Near-field mimo communications for 6g: Fundamentals, challenges, potentials, and future directions," *IEEE Communications Magazine*, vol. 61, no. 1, pp. 40–46, 2022.
- [4] Y. Liu, W. Deng, M. Li, and M.-J. Zhao, "Position-aware beam training for near-field millimeter-wave xl-mimo communications," in *2024 IEEE 99th Vehicular Technology Conference (VTC2024-Spring)*, 2024, pp. 1–6.
- [5] Y. Liu, J. Xu, Z. Wang, X. Mu, and L. Hanzo, "Near-field communications: What will be different?" *arXiv preprint arXiv:2303.04003*, 2023.
- [6] Y. Liu, C. Ouyang, Z. Wang, J. Xu, X. Mu, and A. L. Swindlehurst, "Near-field communications: A comprehensive survey," *arXiv preprint arXiv:2401.05900*, 2024.
- [7] M. K. Samimi and T. S. Rappaport, "3-d millimeter-wave statistical channel model for 5g wireless system design," *IEEE Transactions on Microwave Theory and Techniques*, vol. 64, no. 7, pp. 2207–2225, 2016.

- [8] K. Vuckovic, M. B. Mashhadi, F. Hejazi, N. Rahnavard, and A. Alkhateeb, "Paramount: Towards generalizable deep learning for mmwave beam selection using sub-6ghz channel measurements," *IEEE Transactions on Wireless Communications*, pp. 1–1, 2023.
- [9] M. Cui and L. Dai, "Channel Estimation for Extremely Large-Scale MIMO: Far-Field or Near-Field?" *IEEE Transactions on Communications*, vol. 70, no. 4, pp. 2663–2677, Apr. 2022.
- [10] Y. Zhang, X. Wu, and C. You, "Fast Near-Field Beam Training for Extremely Large-Scale Array," *IEEE Wireless Communications Letters*, vol. 11, no. 12, pp. 2625–2629, Dec. 2022.
- [11] C. Wu, C. You, Y. Liu, L. Chen, and S. Shi, "Two-stage hierarchical beam training for near-field communications," *IEEE Transactions on Vehicular Technology*, vol. 73, no. 2, pp. 2032–2044, 2024.
- [12] G. Jiang and C. Qi, "Near-field beam training based on deep learning for extremely large-scale mimo," *IEEE Communications Letters*, vol. 27, no. 8, pp. 2063–2067, 2023.
- [13] W. Liu, H. Ren, C. Pan, and J. Wang, "Deep learning based beam training for extremely large-scale massive mimo in near-field domain," *IEEE Communications Letters*, vol. 27, no. 1, pp. 170–174, 2023.
- [14] Remcom, "Wireless InSite," <http://www.remcom.com/wireless-insite>.
- [15] A. Ali, N. González-Prelcic, and R. W. Heath, "Millimeter wave beam-selection using out-of-band spatial information," *IEEE Transactions on Wireless Communications*, vol. 17, no. 2, pp. 1038–1052, 2017.
- [16] M. Alrabeiah and A. Alkhateeb, "Deep learning for mmwave beam and blockage prediction using sub-6 ghz channels," *IEEE Transactions on Communications*, vol. 68, no. 9, pp. 5504–5518, 2020.
- [17] W. Deng, M. Li, Y. Liu, M.-M. Zhao, and M. Lei, "Enhancing mmwave beam prediction through deep learning with sub-6 ghz channel estimate," in *2024 IEEE Wireless Communications and Networking Conference (WCNC)*, 2024, pp. 1–6.
- [18] W. Deng, M. Li, M.-M. Zhao, M.-J. Zhao, and O. Simeone, "Csi transfer from sub-6g to mmwave: Reduced-overhead multi-user hybrid beamforming," *IEEE Journal on Selected Areas in Communications*, vol. 43, no. 3, pp. 973–987, 2025.
- [19] H. Wu, L. Lu, and Z. Wang, "Near-field channel estimation in dual-band xl-mimo with side information-assisted compressed sensing," *IEEE Transactions on Communications*, pp. 1–1, 2024.
- [20] V. Vovk, A. Gammerman, and G. Shafer, *Algorithmic learning in a random world*. Springer, 2005, vol. 29.
- [21] A. K. Kuchibhotla, "Exchangeability, conformal prediction, and rank tests," *arXiv preprint arXiv:2005.06095*, 2020.
- [22] A. N. Angelopoulos, S. Bates, A. Fisch, L. Lei, and T. Schuster, "Conformal risk control," *arXiv preprint arXiv:2208.02814*, 2022.
- [23] V. Balasubramanian, S.-S. Ho, and V. Vovk, *Conformal prediction for reliable machine learning: theory, adaptations and applications*. Newnes, 2014.
- [24] A. N. Angelopoulos, S. Bates, M. Jordan, and J. Malik, "Uncertainty sets for image classifiers using conformal prediction," in *International Conference on Learning Representations*.
- [25] B. Wang, M. Zecchin, and O. Simeone, "Mirror online conformal prediction with intermittent feedback," *arXiv preprint arXiv:2503.10345*, 2025.
- [26] J. Chen, S. Park, and O. Simeone, "Knowing when to stop: Delay-adaptive spiking neural network classifiers with reliability guarantees," *IEEE Journal of Selected Topics in Signal Processing*, 2024.
- [27] M. Zecchin, S. Park, and O. Simeone, "Forking uncertainties: Reliable prediction and model predictive control with sequence models via conformal risk control," *IEEE Journal on Selected Areas in Information Theory*, vol. 5, pp. 44–61, 2024.
- [28] K. M. Cohen, S. Park, O. Simeone, and S. Shamai Shitz, "Calibrating ai models for wireless communications via conformal prediction," *IEEE Transactions on Machine Learning in Communications and Networking*, vol. 1, pp. 296–312, 2023.
- [29] M. Zhu, M. Zecchin, S. Park, C. Guo, C. Feng, and O. Simeone, "Federated inference with reliable uncertainty quantification over wireless channels via conformal prediction," *IEEE Transactions on Signal Processing*, vol. 72, pp. 1235–1250, 2024.
- [30] M. Zhu, M. Zecchin, S. Park, C. Guo, C. Feng, P. Popovski, and O. Simeone, "Conformal distributed remote inference in sensor networks under reliability and communication constraints," *arXiv preprint arXiv:2409.07902*, 2024.
- [31] B. Wang, H. Li, S. Shen, Z. Cheng, and B. Clerckx, "A dual-function radar-communication system empowered by beyond diagonal reconfigurable intelligent surface," *IEEE Transactions on Communications*, pp. 1–1, 2024.
- [32] X. Peng, L. Zhao, Y. Jiang, J. Liu, and W. Li, "Channel Estimation for Extremely Large-Scale Massive MIMO Systems in Hybrid-Field Channel," in *2023 IEEE/CIC International Conference on Communications in China (ICCC)*. Dalian, China: IEEE, Aug. 2023, pp. 1–6.
- [33] W. Liu, C. Pan, H. Ren, C.-X. Wang, J. Wang, and X. You, "Nmbenet: Efficient near-field mmwave beam training for multiuser ofdm systems using sub-6 ghz pilots," *IEEE Transactions on Communications*, pp. 1–1, 2024.
- [34] K. Ma, S. Du, H. Zou, W. Tian, Z. Wang, and S. Chen, "Deep learning assisted mmwave beam prediction for heterogeneous networks: A dual-band fusion approach," *IEEE Transactions on Communications*, vol. 71, no. 1, pp. 115–130, 2022.
- [35] G. Zhang, Q. Hu, Z. Qin, Y. Cai, G. Yu, and X. Tao, "A unified multi-task semantic communication system for multimodal data," *IEEE Transactions on Communications*, vol. 72, no. 7, pp. 4101–4116, 2024.
- [36] X. Sun, X. Gao, G. Y. Li, and W. Han, "Single-site localization based on a new type of fingerprint for massive mimo-ofdm systems," *IEEE Transactions on Vehicular Technology*, vol. 67, no. 7, pp. 6134–6145, 2018.
- [37] O. Simeone, "Classical and quantum uncertainty, information, and correlation," <https://sites.google.com/view/osvaldosimeone/cqit>, 2024, in preparation.
- [38] "ReduceLRonPlateau — PyTorch 2.1 documentation." [Online]. Available: https://pytorch.org/docs/stable/generated/torch.optim.lr_scheduler.ReduceLRonPlateau.html
- [39] R. J. Tibshirani, R. Foygel Barber, E. Candès, and A. Ramdas, "Conformal prediction under covariate shift," *Advances in neural information processing systems*, vol. 32, 2019.

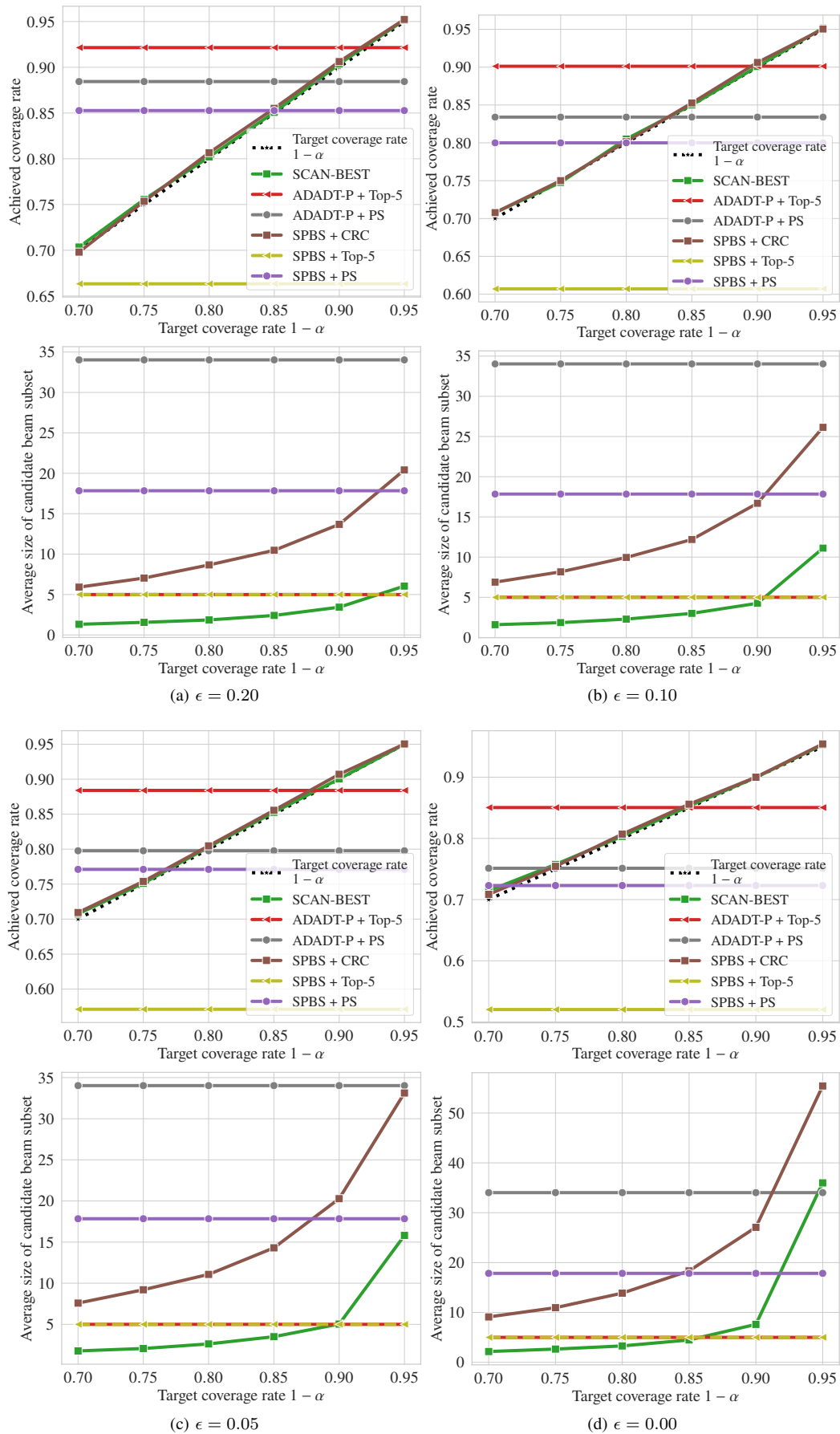


Fig. 11. Achieved coverage rates and average sizes of candidate beam subset of SCAN-BEST and baselines for $\epsilon = 0.20, 0.10, 0.05, 0.00$.